APPLIED SCIENCES AND ENGINEERING

A biomimetically hierarchical polyetherketoneketone scaffold for osteoporotic bone repair

Bo Yuan[1], Linnan Wang[2], Rui Zhao[1], Xi Yang[2], Xiao Yang[1]*†, Xiangdong Zhu[1]*†, Limin Liu[2], Kai Zhang[1], Yueming Song[2], Xingdong Zhang[1]

Copyright © 2020 The Authors, some rights reserved; exclusive licensee American Association for the Advancement of Science. No claim to original U.S. Government Works. Distributed under a Creative Commons Attribution NonCommercial License 4.0 (CC BY-NC).

Osteoporotic fractures are prevalent in society, and their incidence appears to be increasing as the worldwide population ages. However, conventional bone repair materials hardly satisfy the requirements for the repair of pathological fractures. Here, we developed a biomimetic polyetherketoneketone scaffold with a functionalized strontium-doped nanohydroxyapatite coating for osteoporotic bone defect applications. The scaffold has a hierarchically porous architecture and mechanical strength similar to that of osteoporotic trabecular bone. In vitro and in vivo studies demonstrated that the scaffold could promote osteoporotic bone regeneration and delay adjacent bone loss via regulating both osteoblasts and osteoclasts. In addition, the correlations between multiple preimplantation and postimplantation parameters were evaluated to determine the potential predictors of in vivo performance of the material. The current work not only develops a promising candidate for osteoporotic bone repair but also provides a viable approach for designing other functional biomaterials and predicting their translational value.

INTRODUCTION

Polyaryletherketones (PAEKs) are a class of high-performance semicrystalline thermoplastic polymers that have been widely applied to various industrial areas, including the automobile, aerospace, and electronics industries (*1*, *2*). Since its biocompatibility was confirmed and approved by the Food and Drug Administration in 1998, polyetheretherketone (PEEK), a well-known PAEK material, gradually became a leading polymer material used in spinal fusion, joint replacements, trauma repair, and craniomaxillofacial and dental applications because of its excellent mechanical properties, chemical resistance, and natural radiolucency (*3*). However, PEEK often demonstrates poor osteointegration with the host bone, especially under pathological conditions, which hampers its long-term stability and clinical outcomes (*4*). To overcome this deficiency, various strategies, including surface modification and pore structuring, have been developed to enhance the osteointegration of PEEK implants. For example, Liu *et al.* (*5*) incorporated zinc ions into the sulfonated PEEK surface by a magnetron sputtering method. Their results showed that surface-modified PEEK could induce macrophage polarization into an anti-inflammatory phenotype that secretes several osteogenic cytokines to improve osteointegration. Kassick *et al.* (*6*) introduced hydrophilic oxyamine and hydrazine nucleophiles to the diaryl ketone moiety of PEEK via a covalent surface modification strategy, which promoted the osteogenic differentiation and mineralized calcium deposition of MC3T3-E1 cells. Although they exhibited some improved properties, the modification effects of these strategies have been limited to some extent because of the chemical inertness and surface hydrophobicity of PEEK.

In recent years, another representative PAEK material, polyetherketoneketone (PEKK), has received increasing attention in the biomedical field (*7*). In 1994 to 1995, Ho *et al.* (*8*) conducted a series of studies on crystal morphology and phase identification in PAEKs and their copolymers including PEKK. It demonstrated that PEKK has higher thermal stability, better mechanical performance, and more versatile chemical composition compared with PEEK. As a stable supply of implantable-grade raw material produced in recent 20 years became available, PEKK has been gradually used in a variety of medical applications, including spinal fusion and dental and craniomaxillofacial procedures (*9*, *10*). Similar to PEEK, improving osteointegration is vital for the long-term clinical performance of PEKK-based implants. Converse *et al.* (*11*, *12*) developed a hydroxyapatite (HA) whisker–reinforced PEKK porous scaffold by a combined compression molding and particle leaching method. Their result showed that the scaffold with 75% porosity and 20 volume % HA exhibited a mean elastic modulus similar to that of human vertebral trabecular bone (*11*). Recently, Wu *et al.* (*13*) reported a method to create micro/nanostructured surface on silicon nitride/PEKK composite using femtosecond laser. This surface modification could notably enhance in vivo osseointegration and antibacterial activity of the implant (*13*). In our previous studies, we modified the PEKK surface by biomimetic mineralization using the simulated body fluid incubation method (*14*, *15*). Our in vitro and in vivo results confirmed that PEKK containing a higher number of ketone groups allowed easier sulfonation and better bone-like apatite deposition than PEEK without as many ketone groups. This biomineralized PEKK was endowed with a higher bone contact area and bone-bonding strength.

With the acceleration of the aging of the global population, the number of osteoporotic fractures with bone defects has increased markedly (*16*). In China, the number of osteoporotic fractures in 2010 was approximately 2.3 million, with an estimated subsequent increase to 6 million by 2050 (*17*). Compared with normal bone fractures, the repair of osteoporotic fractures is particularly challenging due to their compromised skeletal strength lower density, trabecular microstructure, and bone forming ability, leading to nonunion and fixation failure (*18*). Conventional bone repair materials hardly achieve the desired clinical outcome (*19*). Under osteoporotic conditions, the implant-related failure rate was estimated to

[1]National Engineering Research Center for Biomaterials, Sichuan University, Chengdu 610064, China. [2]Department of Orthopaedics, West China Hospital of Sichuan University, Chengdu 610041, China.
*Corresponding author. Email: xiaoyang114@scu.edu.cn (X.Y.); zhu_xd1973@scu.edu.cn (X.Z.)
†These authors contributed equally to this work.

be approximately 50% (*19*). It has been agreed that implants used in osteoporotic fractures should not only provide mechanically matched support but also favor the surrounding pathological bone to achieve fast osteointegration (*20*). Mimicking the hierarchical microporous structure of natural bone has been considered an effective strategy to facilitate early implant integration with the host bone (*21*), which is essential to support stable fixation in osteoporotic fractures. As the main inorganic constituent of human bone, HA nanoparticles (nHA) play an important role in hard tissue engineering because of its superior biocompatibility and bioactivity (*22*). Synthetic nHA is now used extensively in the form of component or coating of the implants to improve skeletal regeneration (*23*). In 2010, Wang *et al.* (*24*) fabricated a series of nHA-incorporated PEEK nanocomposite materials to achieve an improved mechanical property and bioactivity. Using a compounding and injection molding method, the synthesized nHA were well dispersed in the PEEK matrix without debonding issue (*25*). This method can be adopted to prepare nanocalcium silicate/PEEK bioactive composite as well (*26*). Later, Ma *et al.* (*27*) developed an in situ polymerization approach by first embedding HA fillers in prepolymerized PEEK liquid phase. In a recent study of their research group, a silane coupling agent (KH560) was used for graft modification of nHA and as to prepare nHA/PEEK composites via a hot press molding method (*28*). Johansson *et al.* (*29*) also demonstrated that nHA coating on PEEK implant could significantly promote more new bone formation around the implant and enhance its osteointegration. Inspired by the main component of osteoporotic bone, our group first found that low-crystallinity nHA with a size of 40 to 60 nm could promote the osteogenic ability of osteoblasts primarily derived from osteoporotic bone explants (*30*). Later, we applied this nHA coating onto bioceramic and porous titanium scaffold by vacuum dipping and low-temperature sintering. The layer of nHA coating resulted in a large amount of mature new bone formation, which eventually enhanced the osteointegration of coated implants under osteolytic conditions caused by osteoporosis or bone tumor (*31*, *32*).

Strontium (Sr) used in the form of strontium ranelate drug has been widely used to treat postmenopausal osteoporosis since 2004. Clinical trials confirmed its positive effect of increasing bone mineral density and reducing fracture risk (*33*). However, systematic administration of strontium ranelate is now restricted in many countries because of increased risk of cardiac events. Systematically administered drug will induce an increase in Sr concentration in the blood and cannot effectively reach the bone-implant interface, particularly avascular or necrotic tissue left after surgery (*34*, *35*). Therefore, local release of Sr from implants was expected to achieve a direct absorption by defective tissues in the vicinity. Wong *et al.* (*36*) developed Sr-containing HA/PEEK composites by compression molding technique. Their results indicated that the Sr-containing composites significantly enhanced osteoblast-like cell–mediated mineralization in vitro. Similarly, Li *et al.* (*37*) reported that 10% Sr-substituted HA coating on the surface of titanium could improve implant fixation in osteoporotic bone. We also attempted to incorporate Sr into nHA crystals to further enhance bone resorption inhibition. Injectable Sr-doped nHA (nSrHA) hydrogels and bioceramics were synthesized for this purpose (*35*, *38*). The local release of Sr from nHA balanced bone turnover within the defective area and prevented bone loss near the implant because of continuing osteoporosis.

In the present study, we developed a functionalized biomimetic PEKK scaffold for osteoporotic bone repair with several steps. First, a unique HA microsphere built-in templating method was used to create a well-interconnected macroporous structure. Second, a special sulfonation treatment was applied to endow the scaffold surface with a microporous network. Third, the sulfonation introduced hydrophilic $-SO_3H^-$ groups, which provided multiple nucleation sites for the in situ self-assembly of nHA or nSrHA on the scaffold surface. Last, a hydrothermal treatment was adopted to tailor the grain size and crystallinity of the deposited nanoparticles. In this way, not only was a similar hierarchical bone structure created, but an inorganic phase and mechanical strength close to that of the osteoporotic trabecular bone were also achieved. Osteoporotic osteoblasts and macrophage-derived osteoclasts were used as in vitro cell models to investigate the biocompatibility of the scaffolds. The in vivo performance of the scaffolds was further assessed by implantation in an osteoporotic rat bone defect model. Our results demonstrated that the nSrHA-incorporated PEKK scaffold (nSrHA/PEKK) had a prominent effect on osteoporotic bone defect repair.

RESULTS

Surface characterization and ion release behavior of the scaffolds

Porous PEKK with nHA coating (nHA/PEKK) or nSrHA coating (nSrHA/PEKK) was prepared in three steps, as illustrated in Fig. 1A. Sulfonation treatment was used to introduce hydrophilic $-SO_3H^-$ groups on the pore walls of PEKK, which provided multiple nucleation sites for crystallization of nHA or nSrHA. A hydrothermal treatment was then performed to tailor the grain size, morphology, and crystallinity of the deposited nanoparticles. The as-prepared scaffolds would eventually be implanted into the metaphyseal defects in ovariectomized rat femur to investigate the presumed effect on osteoclasts and osteoblasts (Fig. 1B).

We first characterized the surface morphology of the as-prepared scaffolds by scanning electron microscopy (SEM) to compare it with that of natural osteoporotic bone (Fig. 1C). The surface of the unmodified PEKK was smooth and dense, while a hierarchical microporous network was created by the sulfonation process on the surfaces of the nHA/PEKK and nSrHA/PEKK scaffolds (fig. S1A). Moreover, high-magnification images revealed that this microporous network was covered by uniformly dispersed nHA or nSrHA, which is similar to the osteoporotic bone collagen matrix network embedded beneath osteoblast-secreted nHA. The inserted transmission electron microscopy (TEM) images show that the degraded particles were approximately 50 nm in diameter. The introduction of Sr did not alter the morphology of the nanoparticles. A homogeneous element distribution on the surfaces of various scaffolds was observed. The surface nanotopography of the scaffold was visualized by atomic force microscopy (AFM). As shown in Fig. 1 (D and E), the nanoscale texturing and roughness of nHA/PEKK, nSrHA/PEKK, and osteoporotic bone matrix are similar. Although no difference in the average roughness was observed, the specific surface area (SSA) and hydrophilicity were significantly increased by sulfonation treatment and nanoparticle coating (Fig. 1, F and G). In addition, the similar macroporous structure between the three scaffolds resulted in similar compressive strength (~25 MPa) and elastic modulus values (~0.7 GPa) (fig. S1, B to E), which were comparable to that of trabecular bone in elderly individuals (*39*).

To further verify and quantify the introduced Sr, the surface elemental composition of the samples was analyzed by x-ray photoelectron

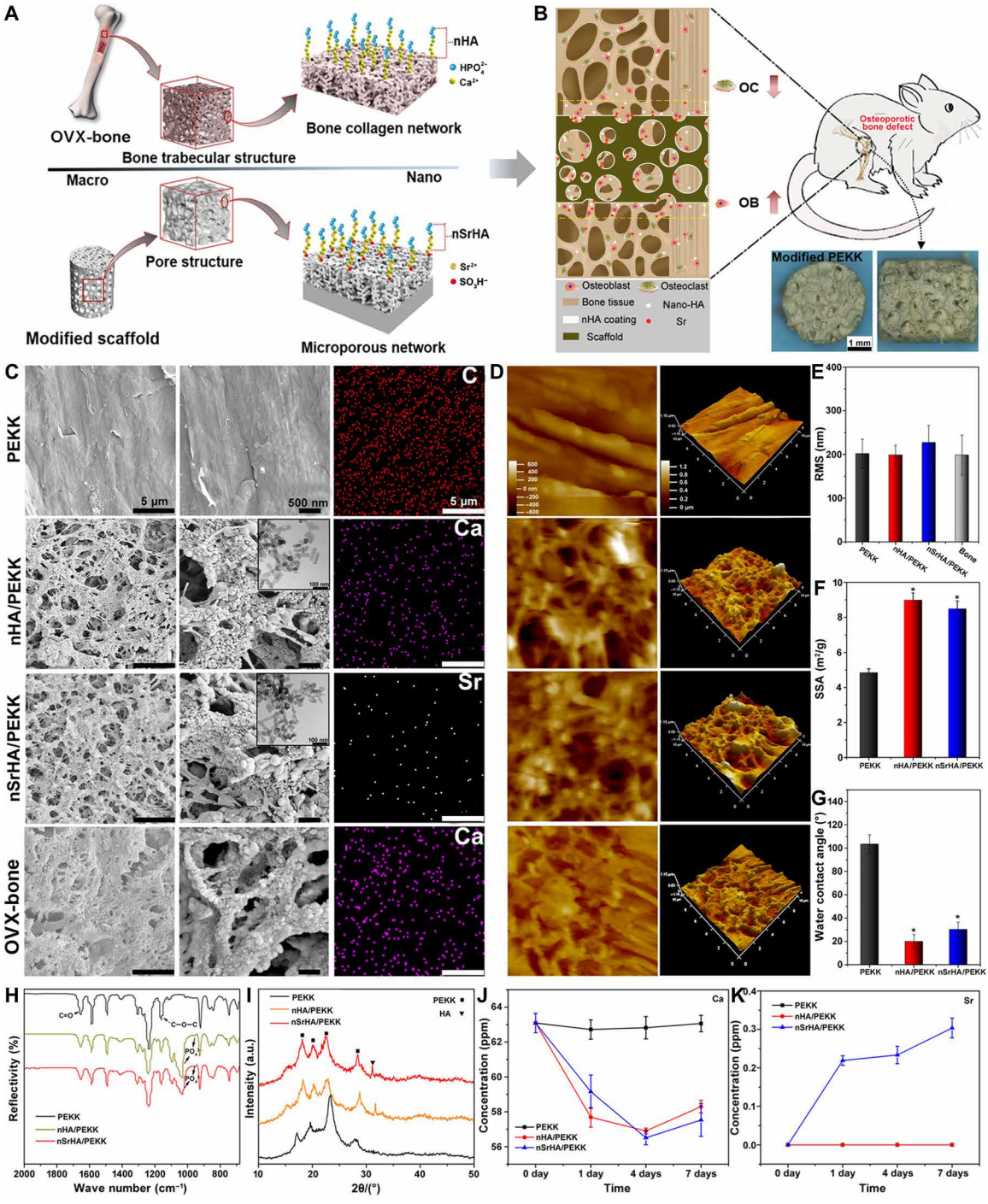

Fig. 1. Preparation and characterization of the biomimetic PEKK materials. (**A**) Schematic illustration of the preparation of biomimetic PEKK scaffold. (**B**) Regulating effect of the biomimetic PEKK scaffold on osteogenesis and osteoclastogenesis of osteoporotic bone defect. OC, osteoclast; OB, osteoblast. (**C**) Typical scanning electron microscopy (SEM) and transmission electron microscopy (TEM) images and element mapping of various PEKK scaffolds and natural osteoporotic bone. (**D**) Atomic force microscopy (AFM) images and corresponding (**E**) surface roughness of PEKK scaffolds and natural osteoporotic bone. (**F**) Specific surface area (SSA) of different scaffolds. (**G**) Water contact angle, (**H**) Fourier transform infrared spectrophotometer (FTIR) spectra, and (**I**) x-ray diffractometer (XRD) patterns of different scaffolds. (**J**) Ca and (**K**) Sr ion release behavior of different scaffolds in cell culture medium (error bars, means ± SD, $n = 3$ per group, $^*P < 0.05$ significant as compared to PEEK, $P < 0.05$ significant as compared to nHA/PEEK). All analyses were done using one-way analysis of variance (ANOVA) with Tukey's post hoc test. Photo credit: Bo Yuan, Sichuan University.

spectroscopy (XPS). As shown in table S1, sulfur (S) was detected on the surface of nHA/PEKK and nSrHA/PEKK, indicating an abundance of $-SO_3H^-$ group products. The replacement ratio of Ca by Sr was 9.7 mole percent (mol %) in nSrHA/PEKK. The Ca/P molar ratio of nHA/PEKK and the (Ca + Sr)/P molar ratio of nSrHA/PEKK were calculated to be 1.66 and 1.67, respectively, indicating the effective replacement by Sr of Ca in the crystal lattice. Fourier transform infrared spectrophotometer (FTIR) and x-ray diffractometer (XRD)

analyses showed that all the samples exhibited the same characteristic bands representing the PEKK materials (Fig. 1, H and I) (*15*). Compared with those of PEKK, the spectra of nHA/PEKK and nSrHA/PEKK contained P—O stretching bands at 960 and 1030 cm^{-1} and C—O asymmetric stretching bands at 1410 and 1460 cm^{-1}. Moreover, according to the XRD patterns shown in Fig. 1I, nHA/PEKK had a typical HA peak (JCPDS 9-0432) at $2\theta = 31.24°$ (*29*), confirming the successful deposition of HA crystalline particles on the sulfonated PEKK. A clear shift of this peak to a lower angle ($2\theta = 31.12°$) was observed in the XRD pattern of nSrHA/PEKK, indicating that Sr was incorporated in the lattice of the HA crystals as a substitute for Ca.

Sustainable Ca and/or Sr ion release was achieved by nHA/PEKK and nSrHA/PEKK scaffolds when immersed in cell culture medium for 7 days (Fig. 1, J and K). In these two groups of scaffolds, the Ca ion concentration measured in the culture medium decreased markedly within 4 days and then slowly increased. This was possibly due to rapid Ca adsorption on the scaffolds and slow Ca release from the nanoparticles. The Ca ion concentration of nHA/PEKK was lower than that of nSrHA/PEKK at day 1, indicating the increased solubility of the nanoparticles with Sr incorporation. We also evaluated the ability of the material to induce bone-like apatite formations in these scaffolds by immersing them in simulated body fluid (fig. S2). This ability was considered to be a critical factor for material-bone integration. Both the nHA and nSrHA coatings remarkably enhanced bone-like apatite formation on the surfaces of the scaffolds.

Osteogenic ability of osteoporotic osteoblasts is elevated by nSrHA/PEKK

To test the potential bone-forming ability of the scaffolds, we cultured them with osteoblasts primarily derived from osteoporotic bone using a previously established protocol from our group (*30*). As shown in Fig. 2A, the osteoporotic osteoblasts cultured on PEKK presented an elongated shape that was attached to the smooth surface by filopodia. However, osteoblasts grown on the nHA/PEKK and nSrHA/PEKK scaffolds showed a flattened polygonal morphology with outstretched lamellipodia anchored to the nanoparticles. Comparatively, a larger cell area was measured in the nSrHA/PEKK group throughout the study period compared with that in the other groups (Fig. 2B and fig. S3). Furthermore, the cell viability of the osteoporotic osteoblasts cultured on nSrHA/PEKK surfaces was significantly higher than that of the other groups (Fig. 2C). We then investigated the effect on key osteogenic gene expressions in osteoporotic osteoblasts cultured with different scaffolds (Fig. 2D). After 14 days of culture, cells in the nSrHA/PEKK group demonstrated strongly up-regulated expression of genes, including alkaline phosphatase (ALP), bone sialoprotein (BSP), runt-related transcription factor 2 (Runx-2), and vascular endothelial growth factor (VEGF). Moreover, the gene expression ratio of osteoprotegerin (OPG)/nuclear factor κB ligand (RANKL) in the nHA/PEKK and nSrHA/PEKK groups was 2.4-fold and 5.3-fold higher than that in the PEKK group, indicating a potential antiosteoclastogenic effect. Western blotting of the secreted protein further confirmed a significantly elevated OPG/RANKL ratio in the nSrHA/PEKK group compared with that in the other groups (Fig. 2E). The participation of several related signaling pathways, including the extracellular signal–regulated protein kinase (ERK), p38, Akt, and β-catenin pathways, was also analyzed by Western blotting. Among the proteins involved in these pathways, phosphorylated ERK (p-ERK) protein levels were significantly enhanced in the nHA/PEKK and nSrHA/PEKK groups (Fig. 2F).

Osteoclastogenesis is inhibited by nHA/PEKK and nSrHA/PEKK

Osteoporosis occurs when osteoclast activity surpasses osteoblast activity (*40*). Thus, in addition to osteogenesis, osteoclastogenesis induced by scaffolds was investigated. First, bone-resorbing multinucleated osteoclasts were derived from macrophage RAW264.7 cells upon RANKL-induced differentiation (fig. S4). The osteoclasts on all three scaffolds maintained a large size and presented ring-like F-actin sealing zones visible by confocal laser scanning microscopy (CLSM) and SEM (Fig. 3, A and B, and fig. S5). The measured number of osteoclasts in the nSrHA/PEKK group was significantly lower than that in the other groups (Fig. 3C). Furthermore, the area with cells that were positive for tartrate-resistant acid phosphatase (TRAP; an enzymatic marker of osteoclasts) in the nHA/PEKK and nSrHA/PEKK groups was significantly smaller than that in the PEKK group (Fig. 3, D and E). The bioactivity of carbonic anhydrase (CAII; a key enzyme involved in bone resorption) and TRAP generated from each group were also detected by an enzyme assay kit. At the end of day 7, the activities of these two enzymes were decreased in the nHA/PEKK and nSrHA/PEKK groups (Fig. 3, F and G).

The expression of key osteoclastic genes, including nuclear factor of activated T cells (NFATc1), cathepsin K (Cath-K), c-fos, matrix metalloproteinase-9 (MMP-9), TRAP, and CAII, was determined (Fig. 3H). Compared with PEKK, the nHA/PEKK and nSrHA/PEKK scaffolds significantly inhibited the expression of these genes, except Cath-K. For the expression of NFATc1, TRAP, and CAII, nSrHA/PEKK exhibited a greater suppressive effect than nHA/PEKK. Together, these results indicated that nHA/PEKK and nSrHA/PEKK not only affected osteoclastogenic gene transcriptional factors (NFATc1 and c-fos) but also altered downstream executive genes (MMP-9, TRAP, and CAII). In accordance with the Western blotting results for osteoblasts, the ERK signaling pathway was also activated in osteoclasts cultured with the nHA/PEKK and nSrHA/PEKK scaffolds (Fig. 3I), with the nSrHA/PEKK group showing the highest p-ERK expression. In addition, nSrHA/PEKK exhibited a stronger inhibitory effect on two master transcriptional regulators related to osteoclast differentiation, c-fos and NFATc1, than nHA/PEKK (Fig. 3J). These results suggested that the ERK pathway played an important role in rebalancing osteoblast and osteoclast activity induced by PEKK surface modifications.

A faster bone turnover rate was induced by nHA/PEKK and nSrHA/PEKK

To investigate the bone regeneration ability of different scaffolds under osteoporotic conditions, cylindrically shaped scaffolds were implanted into metaphyseal defects in ovariectomized rat femurs. We first monitored the changes in body weight and serum bone turnover markers during 12 weeks of implantation. The body weight of the rats increased steadily, and no significant difference was found, whereas serum bone turnover markers differed greatly among the groups (Fig. 4, A to C, and fig. S6, A and B). nSrHA/PEKK resulted in much lower levels of serum bone resorption markers, TRAP and C-terminal telopeptides of type I collagen (CTX). However, the serum levels of the bone formation markers procollagen I N-terminal propeptide (PINP) and osteocalcin (OCN) were both increased in the nHA/PEKK and nSrHA/PEKK groups. These results suggest that the nSrHA/PEKK scaffold can effectively enhance bone formation and inhibit bone resorption.

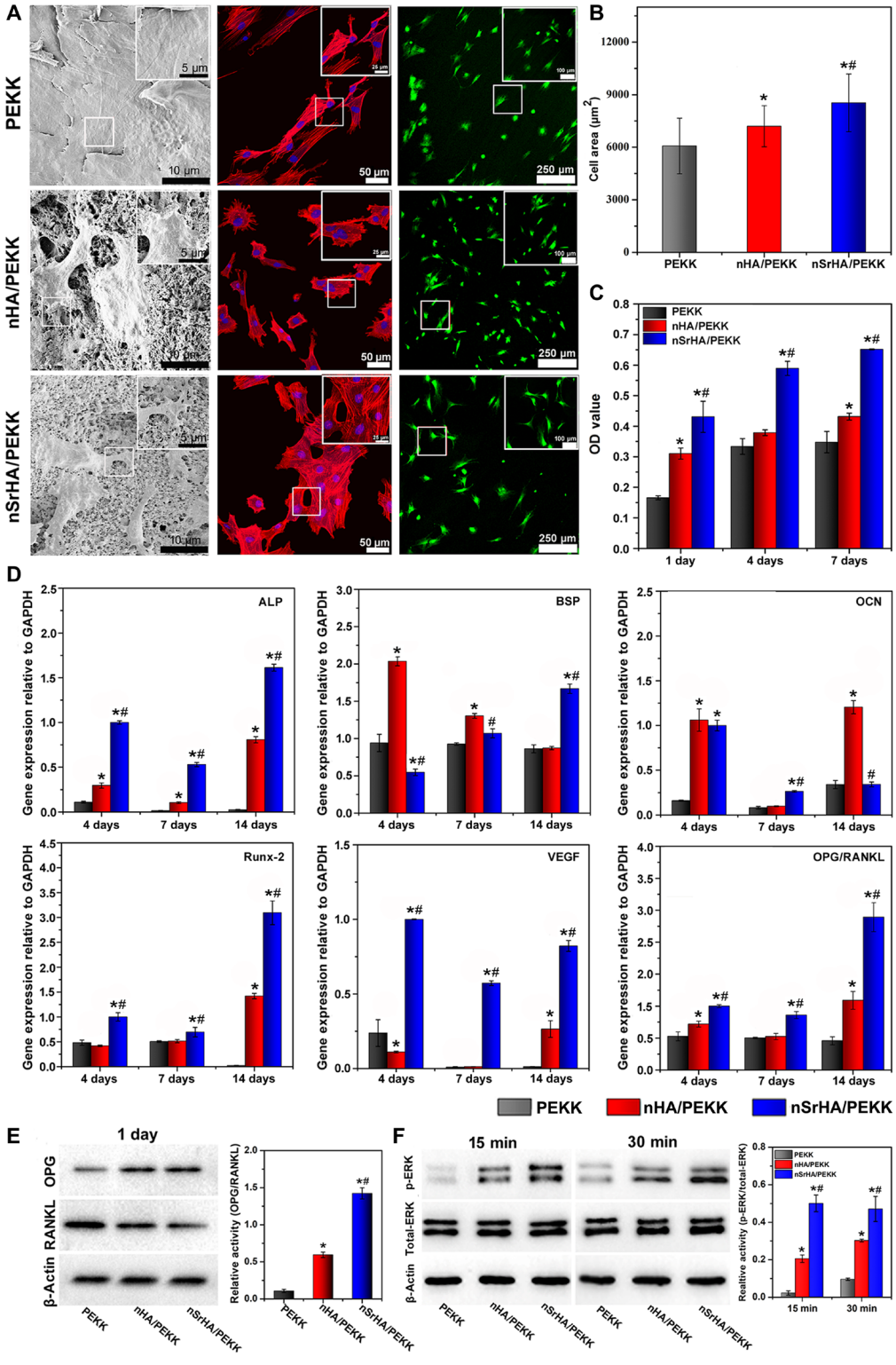

Fig. 2. Effect of various scaffolds on osteogenic ability of osteoporotic osteoblasts. (**A**) SEM and confocal laser scanning microscopy (CLSM) observations and (**B**) the corresponding quantitative assay of the cell area of osteoporotic osteoblasts cultured on different scaffolds for 1 day (actin filament is stained red, while the cell nuclei is stained blue). (**C**) Cell viability of osteoporotic osteoblasts cultured on different scaffolds at days 1, 4, and 7. (**D**) Quantitative reverse transcription polymerase chain reaction (qRT-PCR) analysis for several osteogenic gene expressions of osteoporotic osteoblasts cultured on different scaffolds at days 4, 7, and 14. GAPDH, glyceraldehyde-3-phosphate dehydrogenase. (**E**) Protein expressions of OPG, RANKL, and β-actin measured by Western blotting. (**F**) Protein expressions of total-ERK, p-ERK, and β-actin measured by Western blotting (error bars, means ± SD, $n = 6$ per group for quantitative assay of cell area and $n = 3$ per group for other tests, $^*P < 0.05$ significant as compared to PEEK). All analyses were done using one-way ANOVA with Tukey's post hoc test.

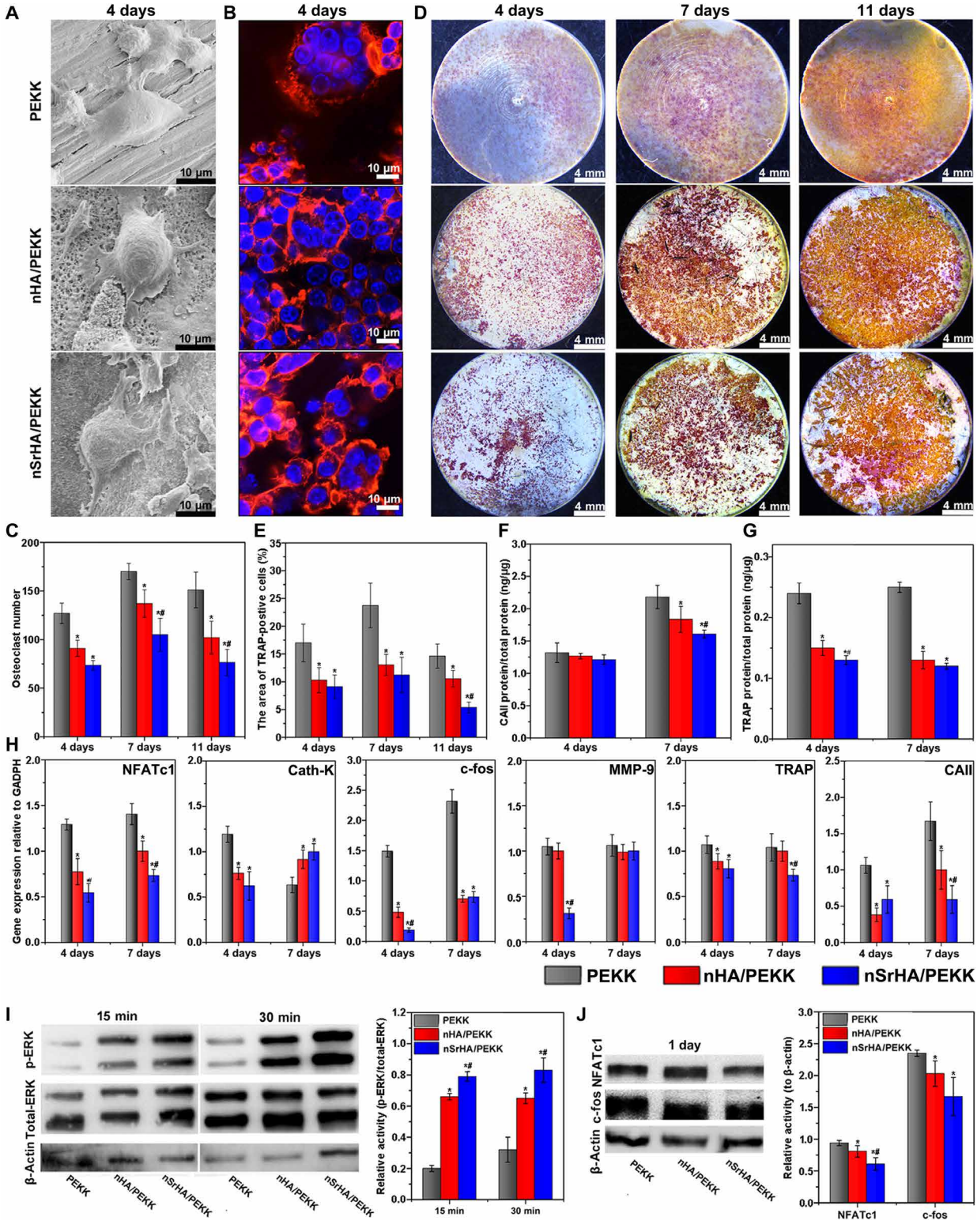

Fig. 3. Effect of various scaffolds on differentiation of RAW264.7 cells to osteoclasts. (**A**) SEM images, (**B**) CLSM observation, and (**C**) cell number quantification of RANKL-mediated RAW264.7 cells cultured on different scaffolds for 4 days. (**D**) TRAP staining and (**E**) positive cell quantification of RANKL-mediated RAW264.7 cells cultured on different scaffolds for 4, 7, and 11 days. (**F**) CAII and (**G**) TRAP protein secretion from osteoclasts of different material groups determined by enzyme-linked immunosorbent assay (ELISA) assay. (**H**) qRT-PCR analysis of essential osteoclastic gene expressions in osteoclasts cultured on various scaffolds at days 4 and 7. Western blotting analysis of (**I**) p-ERK, total-ERK, and β-actin and (**J**) NFATc1, c-fos, and β-actin in osteoclasts cultured on different scaffolds (error bars, means ± SD, $n = 3$ per group, $^*P < 0.05$ significant as compared to PEEK, $\#P < 0.05$ significant as compared to nHA/PEEK). All analyses were done using one-way ANOVA with Tukey's post hoc test.

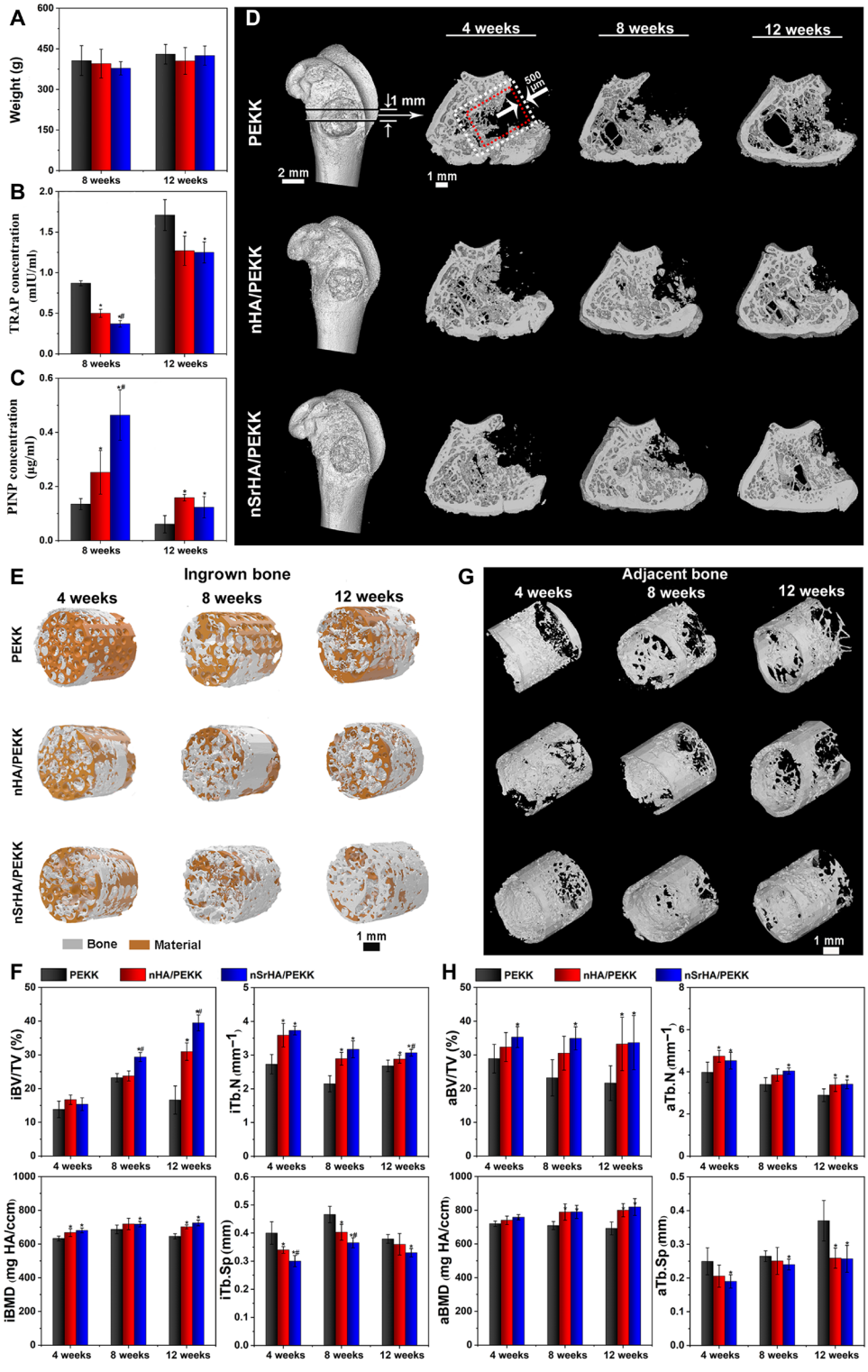

Fig. 4. Serum biomarker measurements and microcomputed tomography (μ-CT) evaluation of osteoporotic bone regeneration induced by different scaffolds. (**A**) Animal weight change, (**B**) serum levels of TRAP, and (**C**) PINP of ovariectomized rats implanted with different scaffolds at weeks 8 and 12 postoperatively. (**D**) μ-CT images showing overall view of the bone specimens and cross-sectional view of the distal femur bone with various scaffold implantation (transparent) at weeks 4, 8, and 12 postoperatively. (**E**) Reconstructed μ-CT images of the newly formed bone (gray) within the porous scaffolds (yellow) and (**F**) μ-CT–rendered parameters of ingrown bone at different time points. (**G**) Reconstructed μ-CT images of the adjacent bone tissue (gray) and (**H**) μ-CT–rendered parameters of adjacent bone at different time points (error bars, means ± SD, $n = 5$ per group, $^*P < 0.05$ significant as compared to PEEK, $\#P < 0.05$ significant as compared to nHA/PEEK). All analyses were done using one-way ANOVA with Tukey's post hoc test.

More ingrown bone was present in the nSrHA/PEKK group, as quantified by microcomputed tomography

The regeneration of new bone inside the implant and the maintenance of the host bone adjacent to the implant were further visualized by microcomputed tomography (μ-CT) (Fig. 4, D to G). Figure 4D shows the cross-sectional view of metaphyseal bone in the defective region. The scaffolds were transparent. More bone formation was observed in the defects of the nHA/PEKK and nSrHA/PEKK groups from week 4 onward. Moreover, the trabecular bone adjacent to the implants was well maintained in these two groups. Because of the development of osteoporosis, severe deterioration of the host trabecular bone structure was found in the inert PEKK group, resulting in an empty hole near the implant at week 12.

A three-dimensionally reconstructed binary μ-CT image of the porous scaffolds with new bone ingrowth is presented in Fig. 4E with respect to the red square area marked in Fig. 4D. Both the nHA/PEKK and nSrHA/PEKK scaffolds (yellow) were enwrapped by a large amount of new bone (gray) at 8 and 12 weeks postimplantation. The ingrown bone volume was quantified and normalized to the total defect volume (iBV/TV). At week 12, the iBV/TV of the nSrHA/PEKK group was 2.5- and 1.3-fold significantly higher than that of the PEKK and nHA/PEKK groups, respectively. In addition, increases in the ingrown bone trabeculae number (iTb.N) and the bone mineral density (iBMD) and a decrease in trabecular separation (iTb.Sp) were measured in the nSrHA/PEKK group. As established in our previous study, the properties of the adjacent bone extending 500 μm from the scaffold surface were considered determinants of bone-implant osseointegration with respect to the area between the red and white squares marked in Fig. 4D (*15*). Figure 4G shows the μ-CT reconstructed ring structure consisting of 0- to 500-μm range of trabecular bone adjacent to the implant. The nSrHA/PEKK group showed a solid composition, while the other groups showed a less dense network. The amount of adjacent bone volume within this ring was quantified and normalized to the total ring volume (aBV/TV). From weeks 4 to 12, the aBV/TV decreased gradually in the PEKK group, while that of the nHA/PEKK and nSrHA/PEKK groups was almost unchanged. The same trend was observed in the adjacent bone mineral density (aBMD) for the different groups. Significantly increased aBMD and adjacent bone trabeculae number (aTb.N) and decreased trabecular separation (aTb.Sp) were found in both the nHA/PEKK and nSrHA/PEKK groups.

Osteoporotic bone regeneration and resorption as confirmed by histological staining

To verify the above μ-CT results, we further analyzed histological staining for the implants retrieved at 4, 8, and 12 weeks postoperatively (Fig. 5A and fig. S6, C and D). Almost all of the pore walls within the nSrHA/PEKK scaffolds were covered by new bone, while less new bone had formed in the inner pores of the PEKK and nHA/PEKK scaffolds at week 12 (Fig. 5A). Other than the changes in new bone formation in the defective area, it is worth noting that the amount of trabecular bone near the PEEK implants remarkably decreased over time because of the progression of osteoporosis (fig. S6C). This deterioration was delayed by the implantation of nHA/PEKK and nSrHA/PEKK. The percentage of ingrown new bone area (iBA/TA) and adjacent bone area (aBA/TA) observed in the histological staining was further quantified (fig. S6E). In accordance with the μ-CT results, from week 8 onward, the iBA/TA of the nSrHA/PEKK group was significantly higher than that of the nHA/PEKK and PEKK groups. In addition, the aBA/TA of the nHA/PEKK and nSrHA/PEKK groups was also higher than that of the PEKK group (fig. S6F).

In the magnified views of the histological samples, a gap can always be found at the interface between the PEKK implant and host bone, as observed by SEM (Fig. 5B). In contrast, a tight bone connection was present at the interface in the nHA/PEKK and nSrHA/PEKK groups. The corresponding energy-dispersive spectrometry (EDS) results further confirmed the formation of new bone and the diffusion of Sr from the nSrHA/PEKK scaffold into the surrounding host bone. In vivo sequential fluorescence labeling with tetracycline and calcein showed a wider distance in the nHA/PEKK and nSrHA/PEKK groups, indicating an increased dynamic mineral apposition rate (Fig. 5C and fig. S6, D and G).

With respect to bone resorption, we performed immunohistological staining of TRAP, OPG, and RANKL at the bone-implant interface (Fig. 5, D to F, and fig. S7). The nSrHA/PEKK group presented significantly fewer TRAP-positive multinucleated cells and a lower osteoclast surface/bone surface ratio than the other groups at all three time points. As mentioned earlier in the in vitro experiment, OPG/RANKL signaling is a classic pathway that determines the fate of osteoclasts. As shown in Fig. 5D, the in vivo protein expression of OPG was found to be highest in the nSrHA/PEKK group among the different groups. Meanwhile, RANKL expression in the PEKK group was significantly higher than that in the nHA/PEKK and nSrHA/PEKK groups. The quantified OPG/RANKL ratio of the nSrHA/PEKK group was much higher than that of the nHA/PEKK and PEKK groups, especially at the early stage of implantation.

Positive effect of the nSrHA/PEKK scaffold on bone strength at the macro- and microlevels

To determine the interfacial bond strength between the scaffolds and the host bone, we performed a macrolevel pull-out test with samples harvested at week 12 (Fig. 6, A to C). The maximum bone-bonding strength and energy absorption to fracture of each sample were determined from the load-displacement curve (Fig. 6A). The averaged maximum load of the nHA/PEKK group was 2.1-fold higher than that of the PEKK group (Fig. 6B). With further incorporation of Sr, the maximum load of the nSrHA/PEKK group was even higher than that of the nHA/PEKK group. In addition, both the nHA/PEKK and nSrHA/PEKK groups showed significantly higher energy absorption than the PEKK group (Fig. 6C). The intrinsic quality of the newly formed bone plays an important role in osteoporotic bone repair (*41*). The nanoindentation technique was further used to probe the ingrown and adjacent bone growth induced by different scaffolds. Programmed loading and unloading were performed continuously on single trabeculae to mimic physiological movements. For ingrown bone and adjacent bone, with an increasing load, typical load-displacement curves were generated, and the changes in the elastic modulus (i*E* and a*E*) and hardness (i*H* and a*H*) were determined (Fig. 6, D and E, and fig. S8). Under the same load, both ingrown and adjacent bone from the nSrHA/PEKK group had the smallest indentation depth of all groups, reflecting a stronger resistance to deformation (*42*). The slope of the load-displacement curve (dotted red line) indicates the stiffness of the bone, which indicates the degree of matrix mineralization (*43*). We observed a lower stiffness according to the curve of the PEKK group, especially for the ingrown bone. In contrast, the nSrHA/PEKK group consistently presented a higher stiffness from shallow to deep indentation. In accordance with our previous studies on bone viscoelasticity (*43*, *44*),

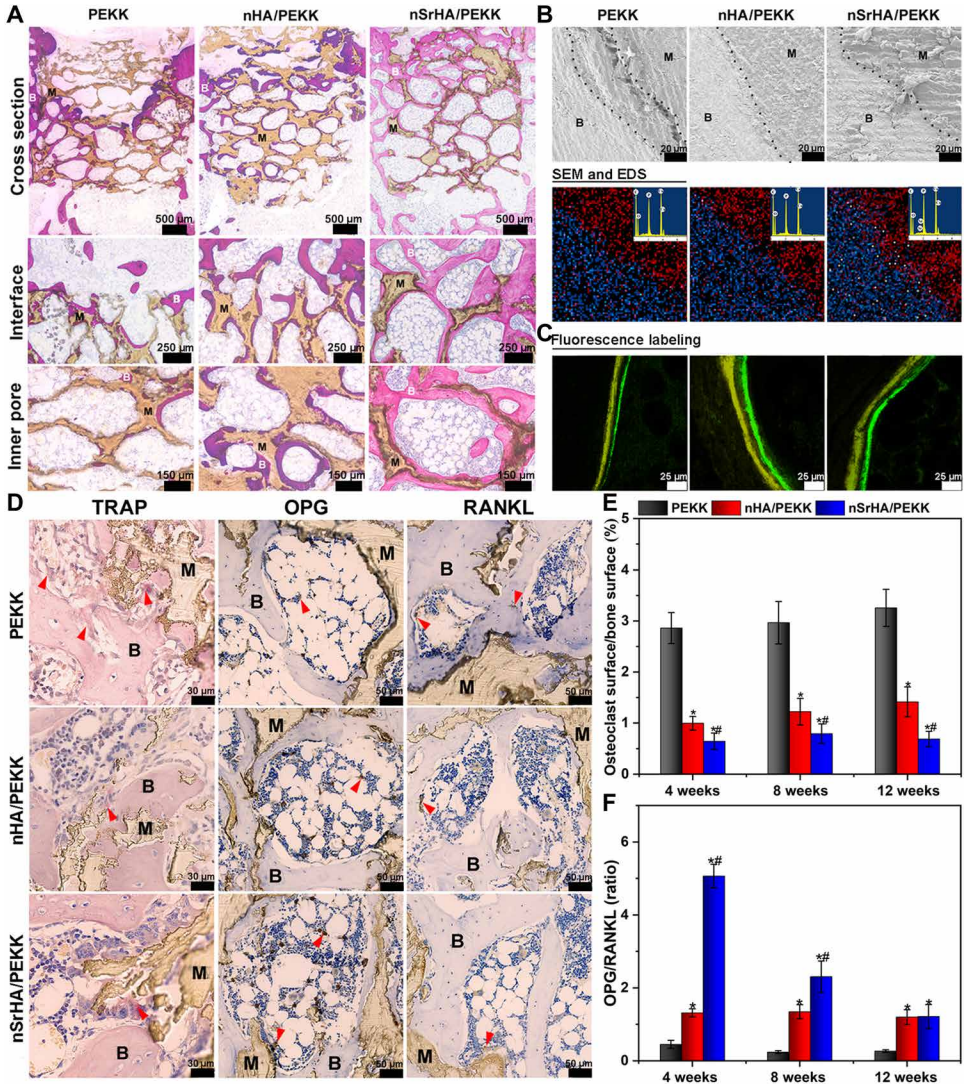

Fig. 5. Histological analysis for osteoporotic bone regeneration and immunohistological analysis for osteoporotic bone resorption induced by different scaffolds. (**A**) Hematoxylin and eosin (H&E) staining of histological sections from different groups at week 12 postoperatively (M, material; B, new bone). (**B**) SEM observation and EDS analysis for the histological sections of the retrieved samples at week 12 (red, carbon; blue, calcium; white, strontium). (**C**) In vivo sequential fluorescence labeling of new bone formation (yellow, tetracycline label; green, calcein label). (**D**) TRAP, OPG, and RANKL staining of histological sections from different groups at week 12 postoperatively (M, material; B, bone tissue; arrow, osteoclast). (**E**) Quantitative analysis of osteoclast surface–to–bone surface ratio and (**F**) OPG-to-RANKL positive staining ratio of the newly formed bone tissue induced by various scaffolds (error bars, means ± SD, $n = 5$ per group, $^*P < 0.05$ significant as compared to PEEK, $^{\#}P < 0.05$ significant as compared to nHA/PEEK). All analyses were done using one-way ANOVA with Tukey's post hoc test.

with an increased load, a general decreasing trend in *E* and *H* for all groups was observed. Typical *E*- and *H*-load curves (fig. S8) and averaged values from indentation depths of 800 to 1000 nm (Fig. 6, F and G) showed that the induced bone in the nSrHA/PEKK group had a higher i*E* and a*E* than that of the PEKK group and a higher i*H* and a*H* than that of the PEKK and nHA/PEKK groups. Together, the results showed that the additive effect of nHA and Sr on macrolevel implant osteointegration arose from the improved intrinsic mechanical strength of both ingrown and adjacent new bone.

Correlation analysis of various osseointegration-related parameters

We rigorously tracked each sample of an identical bulk material from in vitro cell culture to in vivo implantation. After all data were documented, Pearson's correlation analysis was performed to compare the preimplantation and postimplantation parameters (Fig. 6H) (*45*, *46*). We excluded the parameters that were highly observer dependent, including cell number, cell area, positive staining area, bone area, and mineral apposition width. Four regions in the confusion matrix (heatmap) presenting strong correlation coefficients (deep red or blue) were of interest. ① Four osteogenic genes were positively associated with each other, including OCN, RUNX-2, VEGF, and OPG/RANKL. Three osteoclastic genes were also significantly correlated with each other, including NFATc1, Cath-K, and c-fos. ② Among the μ-CT–generated parameters, the ingrown bone indexes iBV/TV, iTb.N, and iBMD were positively associated with each other, indicating the simultaneous enhancement in these aspects of bone quality. In contrast, the adjacent bone aTb.N was not positively

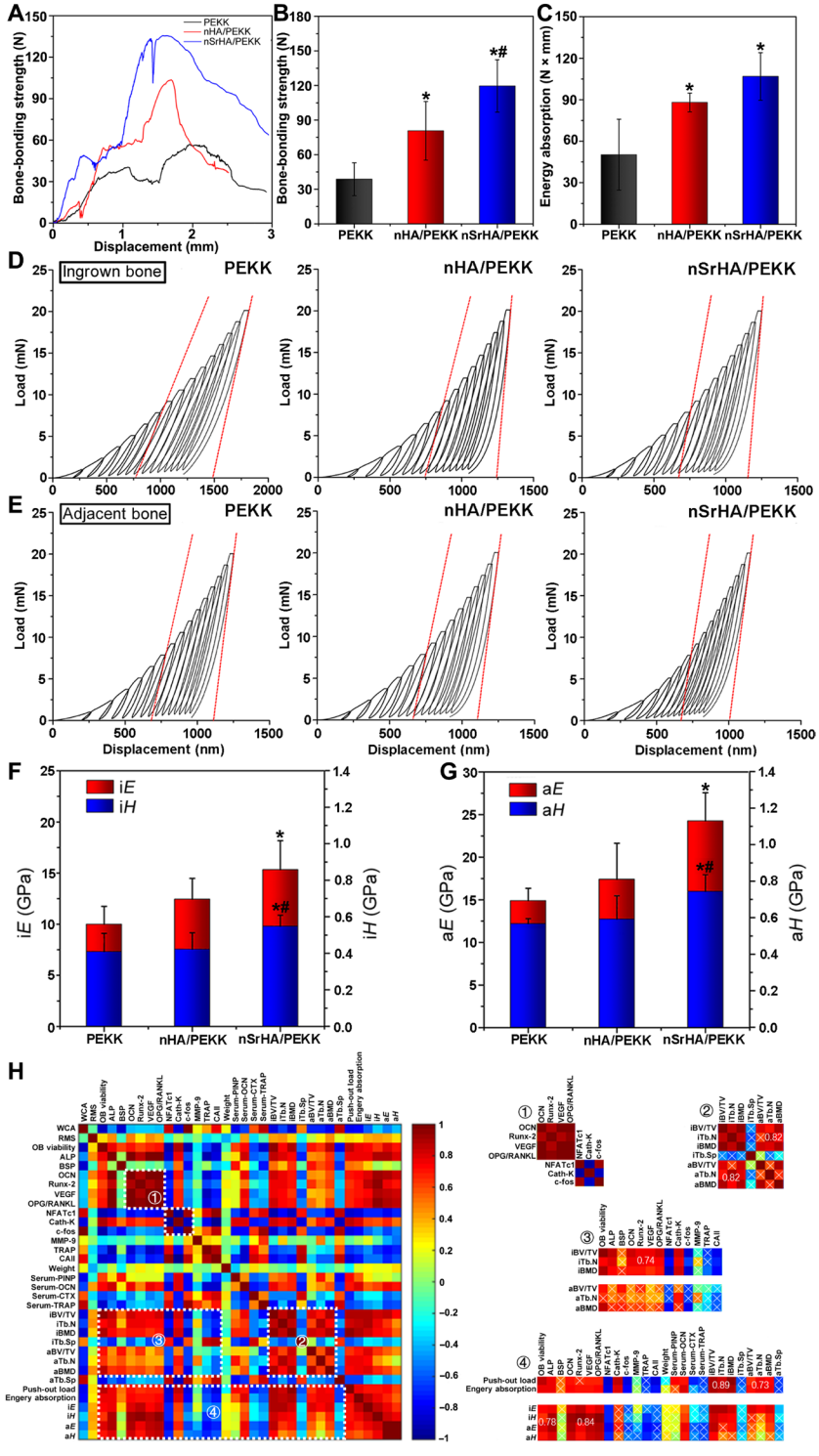

Fig. 6. Effect of different scaffolds on new bone strength at macro- and microlevel and confusion matrix of preimplantation and postimplantation parameters according to their pairwise correlations. (**A**) Typical load-displacement curves, (**B**) maximum load, and (**C**) energy absorption generated from macrolevel mechanical testing of different implants at week 12 postoperatively. (**D**) Typical load-displacement curves generated from cyclic nanoindentation testing on ingrown new bone and (**E**) adjacent new bone (dotted red line, stiffness). (**F**) Averaged i*H* and i*E* calculated from 800- to 1000-nm indentation depth. (**G**) Averaged a*H* and a*E* calculated from 800- to 1000-nm indentation depth. (**H**) The color intensity indicates the magnitude of the correlation coefficient, ranging from −1 to 1 (deep blue to red). Blue and red represents negative and positive correlation. The correlation coefficient was calculated by Pearson's correlation analysis, and significant correlations were identified for *P* values <0.05. Four regions (① to ④) in the matrix represents parameters that were highly correlated, closing to 1 or −1. Cross mark indicates no significant correlation (error bars, means ± SD, $n = 5$ per group, $^*P < 0.05$ significant as compared to PEEK, $\#P < 0.05$ significant as compared to nHA/PEEK). All analyses were done using one-way ANOVA with Tukey's post hoc test.

associated with aBV/TV or iBMD. The cross marks indicate no significant correlation. Furthermore, the ingrown bone indexes were weakly correlated with the adjacent bone indexes, with an average correlation coefficient of 0.82. These two regions of bone formation supported each other. Good osteoconductivity of these porous scaffolds was demonstrated. ③ The ingrown bone indexes were significantly correlated with the expression of the aforementioned osteogenic and osteoclastic genes, while almost no correlation was detected between the adjacent bone indexes and the expression of these genes. This demonstrated that our in vitro osteoporotic osteoblast material culture model can be a useful tool in predicting the outcome of in vivo osteoporotic bone formation preferentially on the pore walls of the scaffold. ④ The overall macrolevel mechanical strength, bone-bonding strength, and energy absorption were strongly correlated with the ingrown bone and the adjacent bone parameters. In comparison, the microlevel mechanical strength, i*E*, a*E*, i*H*, and a*H* were positively associated with osteogenic genes and osteoblast viability and were not significantly correlated with μ-CT–generated ingrown or adjacent bone parameters. First, this result suggested that the stability of a porous implant was more dependent on the amount of bony tissue that extended into the interior than the bone surrounding it. Second, the intrinsic mechanical property of the newly formed bone is highly dependent on the ability of the scaffold to induce osteogenic differentiation to the attached cell.

DISCUSSION

Significant efforts have been expended toward treating clinical osteoporotic defects in recent years (*19*). Despite the substantial progress made in the stable fixation of implants, much less attention has been paid to maintaining bone mass surrounding osteoporotic bone defects. Here, we demonstrated that a biomimetic porous PEKK scaffold with an nSrHA coating could not only promote bone regeneration within the scaffold but also prevent adjacent bone loss from progression of osteoporosis. A dual effect was induced by the nSrHA/PEKK scaffold: the promotion of osteogenesis and the inhibition of osteoclastogenesis both in vitro and in vivo. This dual effect was difficult to achieve even with drug administration to treat osteoporosis. Clinically approved anabolic and antiresorptive drugs are often used concurrently or alternatively, aiming for the additive effects of promotion of bone formation and suppression of bone resorption. However, the clinical outcome of this combination treatment is still controversial (*40*). Previously, we conducted a series of studies that showed that concurrent administration of bisphosphonate and parathyroid hormone (PTH) in osteoporosis might lead to competitive drug antagonism (*43*, *47*). The use of tissue engineering scaffolds to locally alter osteoporotic bone turnover would be a good strategy to circumvent drug antagonism caused by systemic administration.

To mimic the natural osteoporotic bone structure, nSrHA nanoparticles were uniformly dispersed on the microporous network of the sulfonated PEKK surface. Meanwhile, the hydrophilicity and SSA of the scaffold were also significantly enhanced, which was essential for good bioactivity (*48*). Sustainable Sr ion release was achieved by nHA particle degradation. In osteoporotic pathological conditions, osteogenesis is seriously impaired, mainly due to decreased osteoblast activity (*49*). In our previous studies, we proved that nHA promotes the bone-forming function of osteoblasts through the upregulation of endoplasmic reticulum calcium ATPase (adenosine triphosphatase) 2 subunits ATP2A2 and ATP2B2 (*30*, *31*). We also compared the osteoporotic bone regeneration ability of bioceramics with 10% Sr content to that of strontium ranelate drug administration (*35*). Our results suggested that the use of Sr-doped bioceramics would be a much safer choice since abnormally high blood Sr concentrations were found in the drug-treated group.

Commercial osteoblast-like cell lines, i.e., MG63 and MC3T3, are often used to study the biocompatibility of synthetic materials for use in osteoporotic defects. In the present study, we used an osteoblastic cell model that was primarily derived from osteoporotic animal bone explants, which we believe would better reflect cellular responsivity under pathological conditions. The osteoporotic bone explant culture protocol was established earlier (*30*, *31*). In contrast to the healthy osteoblasts derived from sham animals, osteoporotic bone–originated osteoblasts showed significantly lower ALP activity and matrix mineralization ability. Moreover, osteoporotic osteoblasts were more responsive in sensing anabolic treatment than healthy osteoblasts. In the current study, we observed that the nSrHA/PEKK scaffold could significantly increase cell viability, the size of the adhesion area, and expression of most osteogenic genes in osteoporotic osteoblasts. In addition, nSrHA/PEKK and nHA/PEKK significantly increased OPG expression and decreased RANKL expression in osteoblasts at both the gene and protein levels. As a consequence of the net increase in the OPG/RANKL ratio in the nHA/PEKK and nSrHA/PEKK groups, osteoclastogenesis was significantly inhibited. The nSrHA/PEKK group exhibited a much stronger inhibitory effect on osteoclastogenesis, which was reflected by the reduced number of osteoclasts and the down-regulation of transcription factors. The positive role of the ERK pathway in regulating osteoblastogenesis has been generally accepted, whereas its effect in regulating osteoclastogenesis is still controversial (*50*–*52*). In the current study, activation of the ERK signaling pathway was found to play a key role in linking osteoblast and osteoclast activities simultaneously in the nSrHA/PEKK group.

The implantation results further confirmed the dual effect of the nSrHA/PEKK scaffold on bone turnover. In an osteoporotic rat femur defect model, the nSrHA/PEKK implants significantly increased the serum levels of two bone formation markers and decreased the levels of two bone resorption markers compared with those of the PEKK group. At week 12, a large hollow bone marrow area was formed in the metaphyseal region of the PEKK group due to impaired bone regeneration under osteoporotic conditions (*49*). In contrast, a well-maintained adjacent trabecular mesh structure was present in both the nHA/PEKK and nSrHA/PEKK groups. Our μ-CT analysis revealed that the incorporation of Sr and nHA had a positive effect on adjacent bone volume, mineral density, trabeculae number, and separation. Compared with nHA/PEKK, the nSrHA/PEKK scaffold more effectively increased the ingrown bone volume and trabeculae numbers, suggesting the synergistic effect of Sr and nHA. The μ-CT–generated data were confirmed by histological staining, which further indicated that the net gain in ingrown bone in the nSrHA/PEKK group could be ascribed to inhibited bone resorption by osteoclasts in accordance with our in vitro results.

The bonding strength between the host bone and the implant is the gold standard used to assess the degree of implant osteointegration (*53*). A macrolevel mechanical test was thus conducted. Compared with the results of our previous study, the bone-bonding strength of the PEKK scaffold implanted in osteoporotic bone was only approximately 70% of that in healthy bone (*15*). After nHA and nSrHA coating, the maximum load increased two- to threefold. When

viewed at the microlevel, the nanoindentation test results revealed that the nSrHA coating significantly increased the ingrown and adjacent bone hardness compared with the nHA coating, which reflects a greater degree of bone mineralization/matrix maturation (*44*). It was reported that Sr could enter into the hydrated layer in the bone mineral phase and structurally modify the bone matrix to decrease the propagation of microdamage and prevent the fusion of microcracks leading to fractures, hence improving the intrinsic bone tissue quality (*54*, *55*). Compared with our previous nanoindentation test on drug-administered osteoporotic bone, the elastic modulus and hardness of the adjacent trabecular bone surrounding the nSrHA/PEKK implant were 1.7-fold and 1.3-fold greater than those of the PTH and ibandronate combination treatment group, respectively (*47*). This result suggested that the synergistic effects of nHA and Sr released from the implant offered a more efficient way to increase local osteoporotic bone strength than systemic drug treatment.

The development of implant material is often expensive and time-consuming and raises animal ethical issues, and there are instances where the in vitro testing result is inappropriate as a likely predictor of in vivo outcomes (*56*). Correlation analysis has been widely used to identify predictor genes (*57*), histological features (*58*), or CT imaging–generated parameters (*59*), which might be associated with postsurgery survival time or tumor recurrence. Recently, attempts have been made to identify essential preimplantation parameters that predict the in vivo bone-forming capacity of calcium phosphate (CaP)–based bioceramics. These predictor parameters mainly include osteogenic genes (*45*), pathways (*46*), and material properties (*60*), i.e., component and pore structure. These studies shared one common feature in that they designated the bone volume value, as measured by μ-CT, as the implantation outcome to be predicted. For example, a study performed by Chai *et al.* (*45*) found that the high secretion of OPG and bone morphogenetic protein-2 (BMP-2) by cells laden on the material in vitro was associated with the volume of ectopic bone formation in vivo. Bolander *et al.* (*46*) found that early Smad and protein kinase C (PKC) pathway activation predicts the bone-forming capacity of periosteal cells laden with CaP material. In accordance with these results, our Pearson's correlation analysis also revealed that the expression levels of OPG/RANKL and Runx-2 and the downstream gene targets of Smad, PKC, and ERK (*61*) were positively associated with the ingrown bone volume and mineral deposition. Our current study has taken this analysis one step further by distinguishing the ingrown and adjacent bone parameters generated by μ-CT and by setting the mechanical loading capacity of the implant as the ultimate outcome. More specifically, we found that osteogenic genes only predict ingrown bone parameters and intrinsic microlevel mechanical strength of new bone. The macrolevel strength needed to destroy the bone-implant interface is first dependent on the amount and mineralization of the ingrown bone and then on those of the adjacent bone.

In conclusion, we successfully fabricated a biomimetic porous PEKK scaffold for application in osteoporotic bone repair. Our results showed that nSrHA/PEKK has a dual effect in enhancing osteogenesis and inhibiting osteoclastogenesis via the RANKL/OPG and ERK signaling pathways. Not only was new bone formation within the scaffold promoted, but adjacent bone loss due to progression of the disease was also delayed by the scaffold. The intrinsic bone mechanical quality at the microlevel was enhanced by the local release of Sr; thus, the ultimate bonding strength between the scaffold and host bone was greatly improved. We believe that the observed correlations between multiple preimplantation and postimplantation parameters in the current study have significant implications for defining design parameters for the potential therapeutic use of porous material in bone defects. The nSrHA/PEKK scaffold is a promising candidate for osteoporotic bone repair.

MATERIALS AND METHODS

Study design

The objective of this study was to develop a biomimetic PEKK scaffold with nSrHA coating for osteoporotic bone defect applications. Surface topography, composition, porous structure, and mechanical strength were first characterized ($n = 3$). In vitro biocompatibility and osteogenic ability of the nSrHA/PEKK scaffold were examined by coculturing with osteoporotic osteoblasts or osteoclasts. PEKK and nHA/PEKK scaffold were also used and served as control materials ($n = 3$). Cell spreading area, viability, and osteoblastic and osteoclastic marker gene expressions and proteins were measured. Two involved signaling pathways, RANKL/OPG and ERK, were examined. The in vivo performance of the scaffolds was further assessed by implantation in an osteoporotic rat bone defect model. During 12 weeks of implantation, animal weight and serum levels of four bone turnover markers were monitored ($n = 3$). At weeks 4, 8, and 12, the induced effect on new bone regeneration inside and adjacent to the porous scaffold were visualized and quantified by μ-CT and histological staining ($n = 5$). After harvesting all implanted samples, macrolevel mechanical test and nanoindentation test were done to evaluate the degree of implant osseointegration and new bone strength ($n = 5$). Last, the correlations between multiple preimplantation and postimplantation parameters were analyzed to determine the potential predictors of in vivo performance of the material.

Raw materials

Commercially available PEKK powder (Arylmax K7500) was purchased from Polymics Ltd. (State College, PA, USA). The powder was washed sequentially with ethanol and ultrapure water in an ultrasonic cleaner for 30 min before drying at 60°C for 6 hours. Spherical HA microspheres (300 to 800 μm) were supplied by the Engineering Research Center for Biomaterials, Sichuan University, China. Reagent-grade chemicals of pure ethanol, ammonium hydroxide, $Sr(NO_3)_2$, $Ca(NO_3)_2{\cdot}4H_2O$, and $(NH_4)_2HPO_4$ were purchased from Kelong Chemicals (Chengdu, China).

Preparation of sulfonated PEKK

The porous PEKK samples were prepared according to the following procedure. Briefly, HA microspheres and PEKK powder in a 5.5:1 mass ratio were thoroughly mixed with an appropriate amount of ethanol to achieve a slurry. The as-prepared slurry was transferred to a self-prepared mold and sintered at 365°C for 30 min under a pressure of 50 MPa to form a composite. After immersing the composites in 37% HCl solution for 4 hours to leach the HA microspheres, PEKK samples with equivalent pore size and porosity were prepared. Then, the porous samples were immersed in 85% sulfuric acid solution for 30 min and ultrasonically cleaned in deionized water for 15 min to obtain the sulfonated porous PEKK samples. In this study, the PEKK samples with dimensions of $\Phi 14 \times 2$ mm^3 were prepared for material characterization and in vitro study. The porous PEKK samples with dimensions of $\Phi 3 \times 4$ mm^3 were prepared for in vivo animal study.

Synthesis of nHA and nSrHA coatings

In this study, the nSrHA coating with 10 mol % Ca replaced by Sr was synthesized in situ on the microporous network of sulfonated PEKK samples by the chemical precipitation method. The as-obtained sulfonated PEKK samples were transferred to a beaker that contained a solution of $Ca(NO_3)_2$ and $Sr(NO_3)_2$. Then, an appropriate amount of $(NH_4)_2HPO_4$ solution was added dropwise into the beaker according to a (Ca + Sr)/P molar ratio of approximately 1.67. During the process, the pH was constantly adjusted to 10 by adding ammonium hydroxide. After completing the addition of the $(NH_4)_2HPO_4$ solution, the white precipitates containing sulfonated PEKK were further stirred for 2 hours and subsequently treated hydrothermally under an autoclave at 150°C for 12 hours. A layer of nSrHA coated on the microporous network of sulfonated PEKK was obtained after washing in deionized water and anhydrous ethanol several times. A layer of nHA coated on the microporous network of sulfonated PEKK was prepared by the same processing procedure but without the addition of $Sr(NO_3)_2$.

Material characterization

Surface topography of the samples was observed by a field emission SEM (S4800, Hitachi, Japan) equipped with EDS. An AFM (Asylum Research, MFP-3D, USA) operating in tapping mode at ambient conditions was further used to evaluate the surface nanotopography and roughness of the samples. Silicon probes with a resonant frequency of 75 kHz and a force constant of 3 N/m were used. The reported values for the root-mean-square roughness were calculated by averaging the values obtained upon three nonoverlapping sample regions ($10 \times 10\ \mu m^2$). A mercury intrusion porosimetry (AutoPore IV9500, Micromeritics, USA) was used to analyze pore size distribution and porosity of the samples. An FTIR (Nicolet 6700, Thermo Fisher Scientific, USA) equipped with an attenuated total reflection system was used to investigate the surface chemical groups of the samples. Phase composition of the samples was determined by XRD (DX-1000, China). The morphology of HA particles was observed by TEM (Tecnai G^2 F20 S-TWIN, Hitachi, Japan). SSAs of the samples were tested by a surface area and pore size analyzer (Gemini VII 2390t, Micromeritics, USA). Wettability of the samples was detected using a water contact angle measurement machine (lL4200, KRÜSS GmbH, Germany), and parallel tests were carried out on six nonoverlapping area of each sample. Surface elemental composition of the samples was quantified by XPS (XSAM800, Kratos, England) with monochromatic Al Kα radiation source. Three parallel samples of each group were used in the above tests.

Ion release

The samples subjected to sterilization were soaked in 2 ml of Dulbecco's modified Eagle's medium (Gibco, USA) at 37°C for 1, 4, and 7 days. At the prescribed time, all the solution was collected using a pipette. Inductively coupled plasma atomic emission spectroscopy (ICP-AES; IRIS Adv, Thermo Fisher Scientific, USA) was used to quantify the amount of calcium and strontium in the collected medium. For each data point, three parallel samples were used.

Isolation and culture of osteoporotic osteoblasts

All procedures in the experiment were approved by the Institutional Animal Care and Use Committee of Sichuan University. Five female Sprague-Dawley rats aged 8 weeks (200 ± 20 g) were purchased from the Laboratory Animal Center of Sichuan University (Chengdu, China). The detailed procedure for the isolation and primary culture of osteoporotic osteoblasts is listed in the Supplementary Materials and Methods. Osteoporotic osteoblasts from the second passage were seeded on each sample at a density of 5×10^3 per well in 24-well plates and then cultured for 1, 4, 7, and 14 days. The medium was refreshed every 2 days during the culture. All samples were sterilized by 75% alcohol for 1.5 hours and rinsed with sterile phosphate-buffered saline (PBS) twice before the experiment.

Cell morphology and viability

Osteoporotic osteoblasts were seeded on each sample at a density of 5×10^3 per well in 24-well plates and then cultured for 1, 4, and 7 days. RAW264.7 cells (1×10^5 per well) were seeded on various PEKK scaffolds in 24-well plates for 7 days in the presence of RANKL (100 ng/ml). The morphology of cells on different groups of materials was observed by CLSM (Leica TCS-SP5, Germany) and SEM. The mean area of a single cell was quantitatively evaluated by using Image-Pro Plus 6.0 software (Media Cybernetics, USA), in which six randomized nonoverlapping fields in each sample were selected. Cell viability was assessed by the 3-(4,5-dimethylthiazol-2-yl)-2,5-diphenyl tetrazolium bromide (MTT) assay. The details are described in the Supplementary Materials and Methods.

Gene expression

At each time point, RNA was extracted using the RNeasy Mini Kit (Qiagen, Germany) after being washed two times with PBS. Concentration and purity of the extracted RNA were detected using a NanoDrop 2000 UV spectrophotometer (Thermo Scientific, USA). Then, the total RNA was reverse transcribed into cDNA in a 20-μl reaction system using an iScript cDNA synthesis kit (Bio-Rad, CA, USA). The quantitative reverse transcription polymerase chain reaction (qRT-PCR) was performed using SsoFast EvaGreen Supermix (Bio-Rad) in a CFX96 real-time thermocycler (Bio-Rad). The cycling conditions for qRT-PCR are 95°C for 2 min, followed by 40 cycles of 95°C for 2 s and 57°C for 5 s. All experiments were done in triplicate to obtain the average data.

Western blotting

The total protein in cells was isolated at various times. Then, the protein concentration of the lysates was measured using a BCA protein assay kit (Pierce, IL, USA). After heating in boiled water for 10 min in sample buffer (Bio-Rad, USA), equal aliquots of protein (15 mg) were fractionated by 10% SDS–polyacrylamide gel electrophoresis gels (Invitrogen, CA, USA), transferred onto nitrocellulose membranes, and blocked for 1 hour in 1× TBS-T (tris-buffered saline with Tween 20) with 1% bovine serum albumin. After washing three times, the membranes were incubated with primary antibodies against ERK, p-ERK, p38, p-p38, Akt, p-Akt, RANKL, OPG, NFATc1, c-fos, and β-actin (Cell Signaling, MA, USA) overnight and then incubated with a horseradish peroxidase–conjugated secondary antibody (Santa Cruz, CA, USA) at 37°C for 1 hour. A ChemiDoc XRS+ image system with Image Lab software (Bio-Rad, USA) was used to visualize the protein bands, and the protein expression levels were normalized against the level of β-actin for each sample.

TRAP staining, TRAP activity, and CAII activity of RAW264.7 cells mediated by RANKL

RAW264.7 cells (1×10^5) were incubated in α-MEM (α-minimum essential medium) medium supplemented with 10% fetal bovine

serum in 24-well plates in the presence of RANKL (100 ng/ml) (PeproTech, USA). After culture for 4, 7, and 14 days, the cells were stained using a commercially available kit (Sigma-Aldrich, USA). Under the light microscope, cells were counted as osteoclasts if they were stained dark red and contained three or more nuclei. The TRAP and CAII activity of the RAW264.7 cells mediated by RANKL were evaluated quantitatively using a commercially available ELISA (enzyme-linked immunosorbent assay) kit (CUSABIO, China) according to the manufacturer's specifications.

Surgical procedure

The animal experiments were approved by the Institutional Animal Care and Use Committee of Sichuan University. Female Sprague-Dawley rats that received ovariectomy surgery and then further maintained for 12 weeks were used in this study, as previously described (*31*, *35*). Body weight was monitored during the whole implantation time. A distal femoral metaphyseal defect model was established in osteoporotic rats. The detailed surgical procedure is listed in the Supplementary Materials and Methods. The PEKK, nHA/PEKK, and nSrHA/PEKK scaffolds were randomly implanted in the osteoporotic bone defects. Five parallel specimens in each group were tested. At 8 and 12 weeks postoperatively, blood was collected from the rats by a heart puncture, and serum was separated by centrifugation (4000 rpm for 15 min at 4°C). The serum levels of CTX and PINP were assayed using a rat CTX ELISA kit (Cloud-Clone Corp., USA) and a rat PINP ELISA kit (Cloud-Clone Corp., USA) according to the manufacturer's specifications, respectively.

μ-CT analysis

A μ-CT imaging system (SCANCO VivaCT 80, Switzerland) was used to evaluate new bone formation within the defect region of the harvested specimens (n = 5) at 4, 8, and 12 weeks postoperatively. The cross sections of the specimens were imaged by using a scanning procedure with a spot size of 7 μm and a maximum voltage of 70 kV. After being reconstructed with a high-resolution protocol, the resultant grayscale images had an isotropic voxel size of 25 μm (pixel matrix, 2018 × 2048). The obtained grayscale images were further reconstructed and analyzed using the Scanco software. During the reconstruction, a global threshold was used to segment the newly formed bone from each implant. After thresholding and segmentation, the bone volume fractions (iBV/TV and aBV/TV) were evaluated by normalizing the calculated BV to the TV of the area of interest. In addition, the trabecular microarchitecture parameters of the volume of the interest area, including BMD, Tb.N, and Tb.Sp, were assessed by the built-in software of the used μ-CT system.

Histological staining

After μ-CT evaluation, the specimens (n = 5) were dehydrated in ascending concentrations of alcohol from 75 to 100% and then embedded in polymethyl methacrylate. Three transverse sections for each embedded specimen were cut into ~100-μm-thick sections using a microtome (SAT-001, AoLiJing, China), followed by grinding and polishing to a final thickness of ~25 μm. Then, the sections were stained with hematoxylin and eosin (H&E) for histological observation by a light microscope (BX60, Olympus, USA) equipped with a digital CCD (charge-coupled device) camera. For quantitative analysis of newly formed bone, the acquired microscope images were histologically evaluated using Image-Pro Plus software (Media Cybernetics, USA). During the process, the "segmentation" tool was used to quantitatively measure the iBA/TA, which was calculated as the percentage area of new bone in the macropores of the implant, and the aBA/TA, which was defined as the percentage area of bone in the adjacent area. The nonstained sections were observed by CLSM to determine the mineral apposition rate of new bone formation by monitoring the length between the two labels (yellow, tetracycline label; green, calcein label) over time. For quantification of the mineral apposition rate, three randomized nonoverlapping areas in the ingrown bone area of each specimen were analyzed using the IPP 6.0 software.

For TRAP staining, the bone samples with implants were decalcified by immersing samples into decalcifying fluid for 4 weeks. Then, 5-μm-thick sections were cut from the paraffin-embedded tissues to conduct TRAP staining. For the histological detection of RANKL and OPG, sections were dewaxed and hydrated with a gradient. After blocking with 5% hydrogen peroxidase, the sections were incubated with primary antibodies against RANKL and OPG (Cell Signaling, MA, USA). After washing three times, the sections were incubated with secondary antibodies and then avidin-biotin enzyme reagents, followed by counterstaining with hematoxylin. The brown staining around the tissue represents the positive expression of RANKL and OPG, which was observed by a light microscope (BX60, Olympus, USA).

Nanoindentation test

To produce a suitable surface finish for the nanoindentation tests, the samples embedded in epoxy resin were first polished using 320-, 500-, 1200-, and 4000-grit silicon carbide paper, followed by lapping with 3 and 1 μm alumina slurry. Next, the polished samples were ultrasonically cleaned to remove the alumina powder. Immediately after 16 hours of rehydration with 0.9% saline, the samples were subjected to nanoindentation tests using an ultra-nano hardness tester (Anton Paar, Austria) equipped with a Berkovich diamond indenter at room temperature (26°C). Multicycling nanoindentation tests were conducted with an incremental load of 15 cycles. In each cycle, the peak load and the holding time were 20 mN and 5 s, respectively. During the cycle, the samples were first loaded until the peak load of the cycle was reached, partially unloaded by 95% of the load, and immediately reloaded until the next peak load was reached. On the basis of optical microscopic visualization, the indentations were positioned within bone tissue in the adjacent area and ingrown bone area, and three indents were produced in each region, where neighboring indents were spaced more than 60 μm apart. According to the load-displacement curve recorded in each cycle, E and H were measured, and the final measurements were taken at the depth range of 800 to 1000 nm to eliminate the influence of surface roughness in shallow indentations.

Macrolevel mechanical analysis

A macrolevel mechanical test was used to investigate the bonding strength of the bone-implant interface. Before the mechanical test, the newly retrieved bone specimens (n = 5) were cut into cubes and ground to expose the surfaces of the implants. After being ground, the cubes were fixed in a metal support. A material testing machine (Instron 8875, Norwood, MA, USA) was used to perform the mechanical tests. An axial compression load was applied to the implant at a cross-head speed of 1.0 mm/min until the bone-implant interface was ruptured. During the loading process, the load-displacement data were recorded and used to generate the load-displacement

curves, in which the failure load was defined as the maximum bone-bonding load.

Statistical analysis

All data are expressed as the means ± SD of three independent experiments, unless otherwise stated in the caption. Statistical analysis was carried out using the SPSS 16.0 software, and one-way analysis of variance (ANOVA) with Tukey's post hoc test was performed to determine the significant differences between groups. The difference was considered statistically significant at a P value <0.05. Pairwise correlations between preimplantation and postimplantation parameters were investigated using Pearson's correlation analysis for each pair of parameters, and the resulting pairwise correlations were visualized as a confusion matrix. Significant correlations were identified for P values <0.05.

SUPPLEMENTARY MATERIALS

Supplementary material for this article is available at http://advances.sciencemag.org/cgi/content/full/6/50/eabc4704/DC1

REFERENCES AND NOTES

1. S. M. Kurtz, J. N. Devine, PEEK biomaterials in trauma, orthopedic, and spinal implants. *Biomaterials* **28**, 4845–4869 (2007).
2. Q. Dai, Z. Liu, L. Huang, C. Wang, Y. Zhao, Q. Fu, A. Zheng, H. Zhang, X. Li, Thin-film composite membrane breaking the trade-off between conductivity and selectivity for a flow battery. *Nat. Commun.* **11**, 13 (2020).
3. I. V. Panayotov, V. Orti, F. Cuisinier, J. Yachouh, Polyetheretherketone (PEEK) for medical applications. *J. Mater. Sci. Mater. Med.* **27**, 118 (2016).
4. M. Cotic, S. Vogt, S. Hinterwimmer, M. J. Feucht, J. Slotta-Huspenina, T. Schuster, A. B. Imhoff, A matched-pair comparison of two different locking plates for valgus-producing medial open-wedge high tibial osteotomy: Peek–carbon composite plate versus titanium plate. *Knee Surg. Sports Traumatol. Arthrosc.* **23**, 2032–2040 (2015).
5. W. Liu, J. Li, M. Cheng, Q. Wang, K. W. K. Yeung, P. K. Chu, X. Zhang, Zinc-modified sulfonated polyetheretherketone surface with immunomodulatory function for guiding cell fate and bone regeneration. *Adv. Sci.* **5**, 1800749 (2018).
6. A. J. Kassick, S. S. Yerneni, E. Gottlieb, F. Cartieri, Y. Peng, G. Mao, A. Kharlamov, M. C. Miller, C. Xu, M. Oh, T. Kowalewski, B. Cheng, P. G. Campbell, S. Averick, Osteoconductive enhancement of polyether ether ketone: A mild covalent surface modification approach. *ACS Appl. Bio Mater.* **1**, 1047–1055 (2018).
7. A. Amelot, M. Colman, J.-E. Loret, Vertebral body replacement using patient-specific three-dimensional-printed polymer implants in cervical spondylotic myelopathy: An encouraging preliminary report. *Spine J.* **18**, 892–899 (2018).
8. R. M. Ho, S. Z. D. Cheng, B. S. Hsiao, K. H. Gardner, Crystal morphology and phase identification in Poly(Aryl Ether Ketone)s and their copolymers. 4. Morphological observations in PEKK with all p-Phenylene linkages. *Macromolecules* **28**, 5787–5793 (1995).
9. S. Koehler, F. Raslan, C. Stetter, S. M. Rueckriegel, R.-I. Ernestus, T. Westermaier, Autologous bone graft versus PEKK cage for vertebral replacement after 1- or 2-level anterior median corpectomy. *J. Neurosurg. Spine* **24**, 309–314 (2016).
10. J. H. Dawson, B. Hyde, M. Hurst, B. T. Harris, W.-S. Lin, Polyetherketoneketone (PEKK), a framework material for complete fixed and removable dental prostheses: A clinical report. *J. Prosthet. Dent.* **119**, 867–872 (2018).
11. G. L. Converse, T. L. Conrad, R. K. Roeder, Mechanical properties of hydroxyapatite whisker reinforced polyetherketoneketone composite scaffolds. *J. Mech. Behav. Biomed. Mater.* **2**, 627–635 (2009).
12. G. L. Converse, T. L. Conrad, C. H. Merrill, R. K. Roeder, Hydroxyapatite whisker-reinforced polyetherketoneketone bone ingrowth scaffolds. *Acta Biomater.* **6**, 856–863 (2010).
13. H. Wu, T. Liu, Z. Xu, J. Qian, X. Shen, Y. Li, Y. Pan, D. Wang, K. Zheng, A. R. Boccaccini, J. Wei, Enhanced bacteriostatic activity, osteogenesis and osseointegration of silicon nitride/polyetherketoneketone composites with femtosecond laser induced micro/nano structural surface. *Appl. Mater. Today* **18**, 100523 (2020).
14. B. Yuan, Y. Chen, H. Lin, Y. Song, X. Yang, H. Tang, E. Xie, T. Hsu, X. Yang, X. Zhu, K. Zhang, X. Zhang, Processing and properties of bioactive surface-porous PEKK. *ACS Biomater Sci. Eng.* **2**, 977–986 (2016).
15. B. Yuan, Q. Cheng, R. Zhao, X. Zhu, X. Yang, X. Yang, K. Zhang, Y. Song, X. Zhang, Comparison of osteointegration property between PEKK and PEEK: Effects of surface structure and chemistry. *Biomaterials* **170**, 116–126 (2018).
16. N. R. Fuggle, E. M. Curtis, K. A. Ward, N. C. Harvey, E. M. Dennison, C. Cooper, Fracture prediction, imaging and screening in osteoporosis. *Nat. Rev. Endocrinol.* **15**, 535–547 (2019).
17. L. Si, T. M. Winzenberg, Q. Jiang, M. Chen, A. J. Palmer, Projection of osteoporosis-related fractures and costs in China: 2010–2050. *Osteoporos. Int.* **26**, 1929–1937 (2015).
18. C. von Rüden, P. Augat, Failure of fracture fixation in osteoporotic bone. *Injury* **47**, S3–S10 (2016).
19. L. Kyllonen, M. D'Este, M. Alini, D. Eglin, Local drug delivery for enhancing fracture healing in osteoporotic bone. *Acta Biomater.* **11**, 412–434 (2015).
20. S. Ray, U. Thormann, M. Eichelroth, M. Budak, C. Biehl, M. Rupp, U. Sommer, T. El Khassawna, F. I. Alagboso, M. Kampschulte, M. Rohnke, A. Henß, K. Peppler, V. Linke, P. Quadbeck, A. Voigt, F. Stenger, D. Karl, R. Schnettler, C. Heiss, K. S. Lips, V. Alt, Strontium and bisphosphonate coated iron foam scaffolds for osteoporotic fracture defect healing. *Biomaterials* **157**, 1–16 (2018).
21. G. Thrivikraman, A. Athirasala, R. Gordon, L. Zhang, R. Bergan, D. R. Keene, J. M. Jones, H. Xie, Z. Chen, J. Tao, B. Wingender, L. Gower, J. L. Ferracane, L. E. Bertassoni, Rapid fabrication of vascularized and innervated cell-laden bone models with biomimetic intrafibrillar collagen mineralization. *Nat. Commun.* **10**, 3520 (2019).
22. S. M. Zakaria, S. H. Sharif Zein, M. R. Othman, F. Yang, J. A. Jansen, Nanophase hydroxyapatite as a biomaterial in advanced hard tissue engineering: A review. *Tissue Eng. Part B Rev.* **19**, 431–441 (2013).
23. J. Yazdani, E. Ahmadian, S. Sharifi, S. Shahi, S. Maleki Dizaj, A short view on nanohydroxyapatite as coating of dental implants. *Biomed. Pharmacother.* **105**, 553–557 (2018).
24. L. Wang, L. Weng, S. Song, Q. Sun, Mechanical properties and microstructure of polyetheretherketone–hydroxyapatite nanocomposite materials. *Mater. Lett.* **64**, 2201–2204 (2010).
25. L. Wang, L. Weng, S. Song, Z. Zhang, S. Tian, R. Ma, Characterization of polyetheretherketone–hydroxyapatite nanocomposite materials. *Mater. Sci. Eng. A* **528**, 3689–3696 (2011).
26. R. Ma, S. Tang, H. Tan, J. Qian, W. Lin, Y. Wang, C. Liu, J. Wei, T. Tang, Preparation, characterization, in vitro bioactivity, and cellular responses to a polyetheretherketone bioactive composite containing nanocalcium silicate for bone repair. *ACS Appl. Mater. Interfaces* **6**, 12214–12225 (2014).
27. R. Ma, L. Weng, X. Bao, Z. Ni, S. Song, W. Cai, Characterization of in situ synthesized hydroxyapatite/polyetheretherketone composite materials. *Mater. Lett.* **71**, 117–119 (2012).
28. R. Ma, Q. Li, L. Wang, X. Zhang, L. Fang, Z. Luo, B. Xue, L. Ma, Mechanical properties and in vivo study of modified-hydroxyapatite/polyetheretherketone biocomposites. *Korean J. Couns. Psychother.* **73**, 429–439 (2017).
29. P. Johansson, R. Jimbo, Y. Naito, P. Kjellin, F. Currie, A. Wennerberg, Polyether ether ketone implants achieve increased bone fusion when coated with nano-sized hydroxyapatite: A histomorphometric study in rabbit bone. *Int. J. Nanomedicine* **11**, 1435–1442 (2016).
30. R. Zhao, P. Xie, K. Zhang, Z. Tang, X. Chen, X. Zhu, Y. Fan, X. Yang, X. Zhang, Selective effect of hydroxyapatite nanoparticles on osteoporotic and healthy bone formation correlates with intracellular calcium homeostasis regulation. *Acta Biomater.* **59**, 338–350 (2017).
31. R. Zhao, S. Chen, B. Yuan, X. Chen, X. Yang, Y. Song, H. Tang, X. Yang, X. Zhu, X. Zhang, Healing of osteoporotic bone defects by micro-/nano-structured calcium phosphate bioceramics. *Nanoscale* **11**, 2721–2732 (2019).
32. Z. Kun, Z. Yong, X. Cong, Z. Wanlu, W. Hongfeng, T. Jiaoqing, L. Zhongtao, Y. Sen, L. Xiangfeng, M. Li, Y. Zhentao, W. Gang, W. Lin, Z. Kai, Y. Xiao, Z. Xiangdong, T. Chongqi, Z. Xingdong, Application of hydroxyapatite nanoparticles in tumor-associated bone segmental defect. *Sci. Adv.* **5**, eaax6946 (2019).
33. P. J. Meunier, C. Roux, E. Seeman, S. Ortolani, J. E. Badurski, T. D. Spector, J. Cannata, A. Balogh, E. M. Lemmel, S. Pors-Nielsen, R. Rizzoli, H. K. Genant, J. Y. Reginster, The effects of strontium ranelate on the risk of vertebral fracture in women with postmenopausal osteoporosis. *N. Engl. J. Med.* **350**, 459–468 (2004).
34. Y. Xin, J. Jiang, K. Huo, T. Hu, P. K. Chu, Bioactive $SrTiO_3$ nanotube arrays: Strontium delivery platform on Ti-based osteoporotic bone implants. *ACS Nano* **3**, 3228–3234 (2009).
35. R. Zhao, S. Chen, W. Zhao, L. Yang, B. Yuan, V. S. Ioan, A. V. Iulian, X. Yang, X. Zhu, X. Zhang, A bioceramic scaffold composed of strontium-doped three-dimensional hydroxyapatite whiskers for enhanced bone regeneration in osteoporotic defects. *Theranostics* **10**, 1572–1589 (2020).
36. K. L. Wong, C. T. Wong, W. C. Liu, H. B. Pan, M. K. Fong, W. M. Lam, W. L. Cheung, W. M. Tang, K. Y. Chiu, K. D. Luk, W. W. Lu, Mechanical properties and in vitro response of strontium-containing hydroxyapatite/polyetheretherketone composites. *Biomaterials* **30**, 3810–3817 (2009).
37. Y. Li, Q. Li, S. Zhu, E. Luo, J. Li, G. Feng, Y. Liao, J. Hu, The effect of strontium-substituted hydroxyapatite coating on implant fixation in ovariectomized rats. *Biomaterials* **31**, 9006–9014 (2010).

38. B. Yuan, M. G. Raucci, Y. Fan, X. Zhu, X. Yang, X. Zhang, M. Santin, L. Ambrosio, Injectable strontium-doped hydroxyapatite integrated with phosphoserine-tethered poly(epsilon-lysine) dendrons for osteoporotic bone defect repair. *J. Mater. Chem. B* **6**, 7974–7984 (2018).
39. C. Collinge, B. Merk, E. P. Lautenschlager, Mechanical evaluation of fracture fixation augmented with tricalcium phosphate bone cement in a porous osteoporotic cancellous bone model. *J. Orthop. Trauma* **21**, 124–128 (2007).
40. M. R. McClung, Using osteoporosis therapies in combination. *Curr. Osteoporos. Rep.* **15**, 343–352 (2017).
41. Y. Zhu, K. Zhang, R. Zhao, X. Ye, X. Chen, Z. Xiao, X. Yang, X. Zhu, K. Zhang, Y. Fan, X. Zhang, Bone regeneration with micro/nano hybrid-structured biphasic calcium phosphate bioceramics at segmental bone defect and the induced immunoregulation of MSCs. *Biomaterials* **147**, 133–144 (2017).
42. Q. Zhang, S. Gao, J. Min, D. Yu, H. Yu, Graded viscoelastic behavior of human enamel by nanoindentation. *Mater. Lett.* **179**, 126–129 (2016).
43. X. Yang, Y. H. Chan, P. Muthukumaran, S. Dasde, S.-H. Teoh, T. Lee, Ibandronate does not reduce the anabolic effects of PTH in ovariectomized rat tibiae: A microarchitectural and mechanical study. *Bone* **48**, 1154–1163 (2011).
44. X. Yang, S.-H. Teoh, S. DasDe, T. Lee, Administration of PTH and ibandronate increases ovariectomized rat compact bone viscoelasticity. *J. Mech. Behav. Biomed. Mater.* **22**, 51–58 (2013).
45. Y. C. Chai, S. J. Roberts, E. Desmet, G. Kerckhofs, N. van Gastel, L. Geris, G. Carmeliet, J. Schrooten, F. P. Luyten, Mechanisms of ectopic bone formation by human osteoprogenitor cells on CaP biomaterial carriers. *Biomaterials* **33**, 3127–3142 (2012).
46. J. Bolander, Y. C. Chai, L. Geris, J. Schrooten, D. Lambrechts, S. J. Roberts, F. P. Luyten, Early BMP, Wnt and Ca^{2+}/PKC pathway activation predicts the bone forming capacity of periosteal cells in combination with calcium phosphates. *Biomaterials* **86**, 106–118 (2016).
47. X. Yang, P. Muthukumaran, S. DasDe, S. H. Teoh, H. Choi, S.-K. Lim, T. Lee, Positive alterations of viscoelastic and geometric properties in ovariectomized rat femurs with concurrent administration of ibandronate and PTH. *Bone* **52**, 308–317 (2013).
48. R. A. Gittens, L. Scheideler, F. Rupp, S. L. Hyzy, J. Geis-Gerstorfer, Z. Schwartz, B. D. Boyan, A review on the wettability of dental implant surfaces II: Biological and clinical aspects. *Acta Biomater.* **10**, 2907–2918 (2014).
49. F. Marco, F. Milena, G. Gianluca, O. Vittoria, Peri-implant osteogenesis in health and osteoporosis. *Micron* **36**, 630–644 (2005).
50. Y. Zhou, X. Guan, T. Liu, X. Wang, M. Yu, G. Yang, H. Wang, Whole body vibration improves osseointegration by up-regulating osteoblastic activity but down-regulating osteoblast-mediated osteoclastogenesis via ERK1/2 pathway. *Bone* **71**, 17–24 (2015).
51. H. Hotokezaka, E. Sakai, K. Kanaoka, K. Saito, K.-i. Matsuo, H. Kitaura, N. Yoshida, K. Nakayama, U0126 and PD98059, specific inhibitors of MEK, accelerate differentiation of RAW264.7 cells into osteoclast-like cells. *J. Biol. Chem.* **277**, 47366–47372 (2002).
52. F. Chen, M. Wang, J. Wang, X. Chen, X. Li, Y. Xiao, X. Zhang, Effects of hydroxyapatite surface nano/micro-structure on osteoclast formation and activity. *J. Mater. Chem. B* **7**, 7574–7587 (2019).
53. A. H. Poulsson, D. Eglin, S. Zeiter, K. Camenisch, C. Sprecher, Y. Agarwal, D. Nehrbass, J. Wilson, R. G. Richards, Osseointegration of machined, injection moulded and oxygen plasma modified PEEK implants in a sheep model. *Biomaterials* **35**, 3717–3728 (2014).
54. P. Ammann, I. Badoud, S. Barraud, R. Dayer, R. Rizzoli, Strontium ranelate treatment improves trabecular and cortical intrinsic bone tissue quality, a determinant of bone strength. *J. Bone Miner. Res.* **22**, 1419–1425 (2007).
55. D.-G. Kim, S. S. Huja, H. R. Lee, B. C. Tee, S. Hueni, Relationships of viscosity with contact hardness and modulus of bone matrix measured by nanoindentation. *J. Biomech. Eng.* **132**, 024502 (2010).
56. G. Hulsart-Billström, J. I. Dawson, S. Hofmann, R. Müller, M. J. Stoddart, M. Alini, H. Redl, A. El Haj, R. Brown, V. Salih, J. Hilborn, S. Larsson, R. O. Oreffo, A surprisingly poor correlation between in vitro and in vivo testing of biomaterials for bone regeneration: Results of a multicentre analysis. *Eur. Cell. Mater.* **31**, 312–322 (2016).
57. J. Hou, J. Aerts, B. den Hamer, W. van IJcken, M. den Bakker, P. Riegman, C. van der Leest, P. van der Spek, J. A. Foekens, H. C. Hoogsteden, F. Grosveld, S. Philipsen, Gene expression-based classification of non-small cell lung carcinomas and survival prediction. *PLOS ONE* **5**, e10312 (2010).
58. S. M. A. Mahmoud, E. C. Paish, D. G. Powe, R. D. Macmillan, M. J. Grainge, A. H. S. Lee, I. O. Ellis, A. R. Green, Tumor-infiltrating $CD8^+$ lymphocytes predict clinical outcome in breast cancer. *J. Clin. Oncol.* **29**, 1949–1955 (2011).
59. G. J. Li, J. Gao, G. L. Wang, C. Q. Zhang, H. Shi, K. Deng, Correlation between vascular endothelial growth factor and quantitative dual-energy spectral CT in non-small-cell lung cancer. *Clin. Radiol.* **71**, 363–368 (2016).
60. G. Kerckhofs, Y. C. Chai, F. P. Luyten, L. Geris, Combining microCT-based characterization with empirical modelling as a robust screening approach for the design of optimized CaP-containing scaffolds for progenitor cell-mediated bone formation. *Acta Biomater.* **35**, 330–340 (2016).
61. C. J. Logothetis, S.-H. Lin, Osteoblasts in prostate cancer metastasis to bone. *Nat. Rev. Cancer* **5**, 21–28 (2005).

Acknowledgments: We thank L. Chen from the Analytical and Testing Center of Sichuan University for assistance with μ-CT images. **Funding:** This project was funded by the National Key Research and Development Program of China (2016YFC1102000 and 2017YFB0702600), Sichuan Science and Technology Innovation Team of China (2019JDTD0008), Young Elite Scientist Sponsorship Program by CAST (2019QNRC001), Fundamental Research Funds for the Central Universities, "111" Project of China (B16033), Postdoctoral Interdisciplinary Innovation Funds of Sichuan University, project funded by the China Postdoctoral Science Foundation (2020TQ0218).
Author contributions: B.Y., Xiao Yang, K.Z., X. Zhu, and X. Zhang were responsible for the experimental concept, design, and data analysis, and B.Y., Xiao Yang, and X. Zhu wrote the manuscript. B.Y. and R.Z. prepared the materials, performed the studies, and analyzed the data. B.Y., L.L., and Y.S. designed the animal experiments, and B.Y., R.Z., and L.W. performed the animal experiments and analyzed the data. R.Z. and Xi Yang performed μ-CT evaluation and analyzed the data. All authors commented on the manuscript. **Competing interests:** The authors declare that they have no competing interests. **Data and materials availability:** All data needed to evaluate the conclusions in the paper are present in the paper and/or the Supplementary Materials. Additional data related to this paper may be requested from the authors.

Submitted 26 April 2020
Accepted 28 October 2020
Published 11 December 2020
10.1126/sciadv.abc4704

Citation: B. Yuan, L. Wang, R. Zhao, X. Yang, X. Yang, X. Zhu, L. Liu, K. Zhang, Y. Song, X. Zhang, A biomimetically hierarchical polyetherketoneketone scaffold for osteoporotic bone repair. *Sci. Adv.* **6**, eabc4704 (2020).